Quart. J. R. Met. Soc. (1976), **102**, pp. 427–445

551.551.8

A laboratory model of diffusion into the convective planetary boundary layer

By G. E. WILLIS and J. W. DEARDORFF
*National Center for Atmospheric Research, Boulder, Colorado 80303**

(Received 17 July 1975; revised 12 November 1975)

SUMMARY

A laboratory model of the convective planetary boundary layer has provided information concerning the evolution of concentration distributions downwind from a simulated continuous point source located near the ground. Results indicate that a Gaussian plume formulation adequately describes the model y-concentration distributions, but is useful in predicting the z-concentration distributions only to a distance downstream of about $x = 0{\cdot}5z_i/(w_*/U)$, where z_i is the mixed layer depth and w_*/U is a dimensionless stability parameter. Near this distance an elevated concentration maximum appears at a height above the source release height. The elevated maximum rises to a height of about $0{\cdot}8z_i$ at $x = 1{\cdot}7z_i/(w_*/U)$ and retains its identity until the pollutants become vertically well mixed farther downstream. Use of the stability parameter w_*/U permits the model results to be applied to a range of atmospheric conditions encompassing the Pasquill–Gifford stability classes A and B. Close agreement is found between the laboratory data and the atmospheric observations of ground-level lateral spread of Islitzer (1961) and Islitzer and Dumbauld (1963), where the latter measurements extended out to $x \simeq 3$ km.

1. INTRODUCTION

It has recently been demonstrated that through the use of proper scaling parameters the boundary-layer scale turbulence of the clear-air convective planetary boundary layer (or mixed layer) can be realistically simulated by a simple laboratory model (Willis and Deardorff 1974). Modelling simplifications arise when it is noted that the convective turbulence has too short a time scale to be significantly affected by the earth's rotation, and is little influenced by wind shear, which is mainly confined to small heights of several tens of meters (Arya and Wyngaard 1975). This permits the mean wind to be considered as essentially a mechanism for translating downstream the mixed-layer turbulence. With these conditions, the governing parameters for the mixed-layer turbulence have been shown to be (Deardorff 1970) the mixed layer depth z_i; the convective velocity scale $w_* = (g\alpha Q_0 z_i)^{\frac{1}{3}}$, where α is the coefficient of thermal expansion and Q_0 is the kinematic heat flux near the surface; and the convective temperature scale, $T_* = Q_0/w_*$.

The laboratory model consists of penetrative convection (with zero mean wind) of a deep fluid layer heated from below into an overlying stable layer. A complete description of the laboratory convection chamber is given in Willis and Deardorff (1974). The chamber utilizes water as the working fluid and has a horizontal area of $114 \times 122\,\text{cm}^2$. The sidewalls are of plexiglass to allow both lighting and viewing of the chamber interior. The lower-boundary heating rate and mixed-layer depth were made sufficiently large to ensure that the convective flow was highly turbulent. For the experiments to be described in this paper, two values of typical mixed-layer depths were used, 29 and 60 cm.

Considering the absence of comprehensive diffusion measurements within the atmospheric mixed layer, and the dim prospects of obtaining such data economically over scales of many kilometers, attention has turned to the use of numerical and physical models of the convective boundary layer A three-dimensional numerical boundary-layer model of

* The National Center for Atmospheric Research is sponsored by the National Science Foundation.

Deardorff (1972) has provided statistics on the vertical spread of neutrally buoyant particulates from a plane source located near the surface. Comparison between the laboratory and numerical model results will be seen to provide information regarding the choice of horizonal aspect ratio for the laboratory experiments. Lamb *et al.* (1974) have made use of Deardorff's numerical model to calculate concentration distributions in the $x-z$ plane, where x is the co-ordinate aligned with the mean wind, and also have provided information concerning the lateral spread of particulates.

Laboratory model results of the vertical diffusion from an instantaneous line source (ILS) near the surface have been reported by Deardorff and Willis (1974a). The vertical spread of particulates or pollutants was followed from soon after release until they were uniformly distributed throughout the mixed layer. The purpose of this paper is to extend the previous laboratory study to the simulation of diffusion from a continuous point source (CPS) into a mixed layer having uniform mean wind U, and to report on the lateral as well as the vertical diffusion.

2. Methods of measurements and data analysis

Since the bulk of the results to be presented in this paper pertain to the experiments when $z_i \simeq 29$ cm, the description of methods in this section will refer to that case. Similar methods were used when $z_i \simeq 60$ cm with different values of certain parameters that can be noted by reference to Table 1. In Table 1 the term l/z_i is the aspect ratio of horizontal length between chamber sidewalls relative to the mixed-layer depth. The quantity z_r is the average height of particle release and z_d is the maximum height to which the diffusion extended. It is to be understood that the quantities presented in Table 1 are averages over the length of time of diffusion measurements and over the ensemble of experiments in each case.

TABLE 1. Values of similarity parameters and other pertinent experimental data

Case	Number of experiments	z_i (cm)	w_* (cms^{-1})	Q_0 (cms^{-1} degC)	l/z_i	z_r/z_i	z_d/z_i	Average number of particles per experiment
1	7	28·7	0·98	0·135	4·0	0·067	1·13	1150
2	5	59·9	1·22	0·128	1·9	0·050	1·10	1630

The initial filling of the tank, stratification of the stable layer, and measurements of boundary conditions were performed in a manner similar to that described in Willis and Deardorff (1974). The particulate tracers used were neutrally buoyant oil droplets with average diameter 0·8 mm. The particles were illuminated from opposite sides of the chamber and photographs of the particle distributions were taken from the front.

The experimental procedure was to apply heat to the lower boundary to initiate the convection; allow several minutes waiting period to permit the convection to become fully established; introduce the particles along a centre line extending the length of the chamber at $z_r = 0{\cdot}067 z_i$; and then photograph the spreading (laterally in y and vertically in z) particle distribution at 2–5 second intervals until particles had reached the vicinity of the sidewalls. The camera height was fixed at approximately $0{\cdot}5 z_i$, and its view of the y–z plane was end-on to the initial line of particles. Approximately a 4-second release time was required to lay down the 'instantaneous' line of about 1150 particles. During measurements of particle diffusion the dimensionless entrainment rate $(1/w_*)\partial z_i/\partial t$ had

average values in the range 0·010–0·015, which allowed ample time (about 2 minutes) for the diffusion measurements before z_i had increased by 5%.

A series of such experiments was performed, from which 7 were sufficiently complete in data to be used in the analysis. The photographic data were reduced by projecting the photographs on a grid of squares each of area $\Delta y \Delta z = (0{\cdot}067 z_i)^2$. Particles in each square were counted and normalized by the total number visible in each photograph. Subsequent averaging of particle counts from the 7 experiments and calculation of statistics of the particle distributions were done by digital computer. Unless otherwise noted, the results presented in this paper will represent the average over the ensemble of experiments.

The data have been corrected for camera parallax and refraction at the chamber air–water interface (the displacement of rays due to the plexiglass front wall was neglected). Corrections applied to the y-distributions were generally less than 5% and were not applied beyond times when the average correction was less than 2%. Corrections for the z-distributions were larger, amounting to 21% average change for the lowest layer $0 < z < 0{\cdot}067 z_i$ and 5% change for the next higher layer. Corrections were smaller at higher levels except when concentration gradients were large.

Corrections have also been applied to the r.m.s. spreads in y and z for the effects of finite source-release time and finite grid interval. The combined corrections in y amount to about -8% for the first measurement after release and diminish to less than -2% by the fourth measurement. The corrections in z were about one-half those in y.

3. Transformation to a simulated point source

A single photograph of particles gives an instantaneous view of the particle distribution in the y–z plane integrated along the line-of-sight x axis as in Fig. 1. The full series of

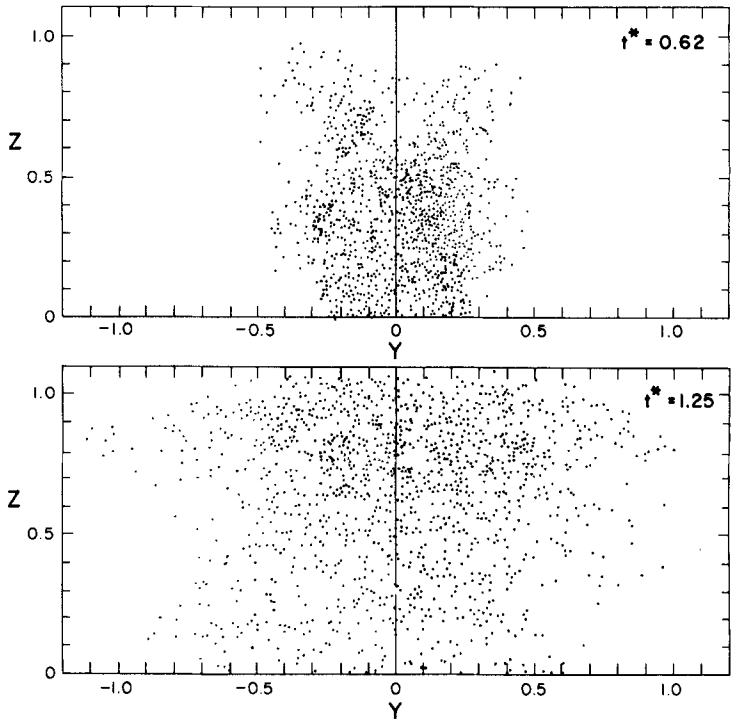

Figure 1. Photographic view of particles diffusing in the Y–Z plane from an individual experiment of case 1 for $t^* = 0{\cdot}62$ and $1{\cdot}25$. The chamber sidewalls are located at $Y = \pm 2$.

photographs displays how the particles diffuse in time from an ILS. Fig. 1 depicts two distributions of the diffusing particles as viewed by the camera from an individual experiment of case 1 when $t^* = 0{\cdot}62$ and $1{\cdot}25$ (defined below). By the time $t^* = 0{\cdot}62$ some particles have diffused vertically to near the top of the mixed layer and when $t^* = 1{\cdot}25$, the lateral spread of particles is continuing while the vertical spread has been limited by the influence of the overlying stable layer.

The appropriate dimensionless time t^* for this system is given by

$$t^* = (w_*/z_i)t \quad . \quad . \quad . \quad . \quad (1)$$

where t is measured from the centred time of particle release. A transformation from the ILS to a simulated CPS in the presence of a uniform mean wind U blowing along the x co-ordinate can be made by assuming that Taylor's hypothesis of $t \rightarrow x/U$ is valid for this system. This assumption implies that diffusion in the downstream direction from the CPS is negligible in comparison with the effect of mean advection, which is consistent with the absence of (downstream) diffusion along the axis of the ILS. Replacement of t in (1) by x/U leads then to a dimensionless distance, X, given by

$$X = (w_*/U)(x/z_i) = t^* \quad . \quad . \quad . \quad (2)$$

where $X = 0$ is the location of the CPS. Here t^* is regarded as the dimensionless downstream travel time following particle release. The limitations on applicability of this approach have been estimated to be (Deardorff and Willis 1974b)

$$1{\cdot}5w_* \leqslant U \leqslant 6w_*. \quad . \quad . \quad . \quad . \quad (3)$$

The lower limit refers to breakdown of Taylor's translation hypothesis due to too weak a mean wind. The upper limit refers to breakdown of the assumption that the turbulence causing the diffusion in the bulk of the boundary layer is produced much more by the buoyancy force than by shear stress.

4. Dimensionless concentrations

The main results of this study will be presented in terms of a dimensionless concentration C derived from the particle counts. Let the number of particles at any given time viewed in a square $\Delta y \Delta z$ be denoted by n_{jk}, where j and k refer to the location of each square in the y–z plane. Let N be the total number of particles in each photograph, and $\mathscr{L}$ be the length of the ILS along the x direction. Then the number density or concentration c (number/unit volume) projected onto a given square can be written

$$c = n_{jk}/\mathscr{L}\Delta y \Delta z. \quad . \quad . \quad . \quad (4)$$

The ILS strength (number emitted/unit length) is simply $N/\mathscr{L}$, and is related to an equivalent CPS strength S (number emitted/unit time) and to U by

$$N/\mathscr{L} = S/U. \quad . \quad . \quad . \quad . \quad (5)$$

Combining (4) with (5), a dimensionless concentration C can be written as

$$C(X, Y, Z) = c(X, y, z)z_i^2 U/S \quad . \quad . \quad . \quad (6)$$

where $Y = y/z_i$, $Z = z/z_i$, and X is given by Eq. (2).

5. Results and discussion

Short- and long-range time limitations on the usefulness of the concentration data are

imposed by the laboratory equipment and experimental techniques. For case 1 (see Table 1) the long-range limitation occurs at $X > 3$ when some of the particles have diffused to positions near the sidewalls. The short-range limitations are imposed by the length of time required to lay down the initial line ($t^* \simeq 0{\cdot}13$) and the difficulty in obtaining accurate particle counts at early times when the number of particles per unit volume is great. Hence the present results will be confined to the downstream region

$$0{\cdot}13 < X < 3{\cdot}0 \qquad . \qquad . \qquad . \qquad (7)$$

(*a*) *Vertical and lateral spread*

Let the height of an individual particle be z_p. If z_p is averaged over all particles and made dimensionless by z_i, it becomes the dimensionless mean particle height, $\bar{Z}_p$, or vertical centre of mass of the diffusing particles. This quantity was calculated by use of

$$\bar{Z}_p = \int_0^{z_d} Z_p P_z \, dz \qquad . \qquad . \qquad . \qquad (8)$$

where $P_z\,dz$ is the probability that a particle exists in the horizontal layer between $z-\frac{1}{2}\Delta z$ and $z+\frac{1}{2}\Delta z$. Values of $\bar{Z}_p$ as a function of X are shown in Fig. 2 for both cases 1 and 2. The particle centre of mass rises from the release height to a value of $0{\cdot}5z_i$ by $X = 0{\cdot}9$,

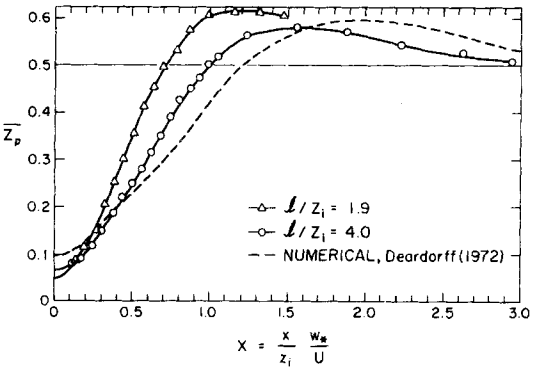

Figure 2. Dimensionless mean particle height as a function of distance downstream from release point. Dashed curve is from the numerical calculations reported in Deardorff and Willis (1974a).

overshoots the asymptotic value by about $0{\cdot}1z_i$, and then approaches it in a series of damped oscillations that continue far downstream (Deardorff and Willis 1974a). The dashed curve in Fig. 2 is from the large Reynolds-number numerical calculations of Deardorff (1972, Fig. 29) in which $l/z_i = 4$ and $z_r = 0{\cdot}1z_i$.

The overall dimensionless vertical standard deviation of particle displacement is defined as

$$(\overline{Z_p'^2})^{\frac{1}{2}} = \left[\int_0^{z_d} (Z-Z_r)^2 P_z \, dz\right]^{\frac{1}{2}} . \qquad . \qquad . \qquad . \qquad (9)$$

Similarly the dimensionless overall lateral standard deviation of particle displacement is

$$(\overline{Y_p'^2})^{\frac{1}{2}} = \left[\int_{-l/2}^{l/2} Y^2 P_y \, dy\right]^{\frac{1}{2}} \qquad . \qquad . \qquad . \qquad (10)$$

where $P_y\,dy$ is the probability that particles anywhere in a vertical column occur between $y-\frac{1}{2}\Delta y$ and $y+\frac{1}{2}\Delta y$. Y_r does not appear in (10) since the release line defines $Y = 0$.

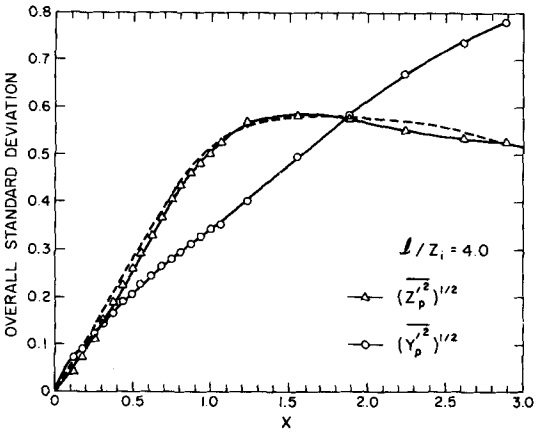

Figure 3. Dimensionless overall particle standard deviations as a function of distance downstream for a horizontal aspect ratio of 4. Dashed curve is from numerical calculations of $(\overline{Z_p'^2})^{\frac{1}{2}}$ reported in Deardorff and Willis (1974a).

The vertical and lateral spreads are plotted versus X in Fig. 3 for $l/z_i = 4$ and in Fig. 4 for $l/z_i = 1{\cdot}9$. The dashed curves in both figures represent values of $(\overline{Z_p'^2})^{\frac{1}{2}}$ from numerical calculations of Deardorff (Deardorff and Willis 1974a) in which $l/z_i = 4$ and $z_r = 0{\cdot}1z_i$. Results as plotted in Fig. 3 indicate that when $z_r = 0{\cdot}067z_i$ the particles spread at approximately equal rates along Y and Z out to $X \simeq 0{\cdot}3$ where the spread in Z becomes larger. For short distances downstream a linear growth rate expressed by $(\overline{Z_p'^2})^{\frac{1}{2}} = (\sigma_w/w_*)X$ can be expected for the elevated source. In the region $0{\cdot}2 < X < 0{\cdot}8$ the average vertical spread turns out to be closely proportional to $X^{1{\cdot}15}$ as compared with the $X^{1{\cdot}5}$ prediction of Yaglom (1972) for a ground release. The remaining degree of vertical 'acceleration' (exponent of 1·15 instead of 1·50) we attribute to the effect of our source height being at a level well below the maximum in the σ_w profile. The limiting effect of the overlying stable layer becomes apparent by $X \simeq 0{\cdot}8$ as the vertical spread slows. An overshoot occurs as in Fig. 2 for $\overline{Z}_p$, as the large-scale eddies carry more particles higher up into the mixed layer, leaving the lower layers somewhat deficient in particles. Subsequently, $(\overline{Z_p'^2})^{\frac{1}{2}}$ slowly approaches its asymptotic value of about 0·5 as the large-scale eddies return more particles to lower levels and the concentration approaches a more uniform vertical distribution.

The values of $(\overline{Y_p'^2})^{\frac{1}{2}}$, while continually increasing with X, do not display the curvature expected of Taylor's long-range prediction $(\overline{Y'^2})^{\frac{1}{2}} \propto X^{\frac{1}{2}}$ until X exceeds the rather large value of about 2. This behaviour appears to be associated with retarded lateral diffusion in the region $0{\cdot}6 < X < 2{\cdot}0$, the particles being partially trapped for a length of time in the lateral confines of the large-scale eddies into which they were released. The average lateral spread in the region $0{\cdot}2 < X < 0{\cdot}8$ can be approximated by $(\overline{Y_p'^2})^{\frac{1}{2}} = 0{\cdot}38X^{0{\cdot}83}$.

The $(\overline{Y_p'^2})^{\frac{1}{2}}$ values for $l/z_i = 1{\cdot}9$ in Fig. 4 are in close agreement with those for $l/z_i = 4$. However, $(\overline{Z_p'^2})^{\frac{1}{2}}$ increases faster than for the larger aspect ratio of case 1 and the first limiting effects of the capping inversion on the vertical spread are noticeable by $X \simeq 0{\cdot}6$. While the limiting effect of the stable layer on the vertical spread of particles is felt at a smaller distance downstream for the smaller aspect ratio, the magnitude of the overshoot is somewhat enhanced.

Because of the closer agreement between the numerical calculations and the measured values of $\overline{Z}_p$ and $(\overline{Z_p'^2})^{\frac{1}{2}}$ for case 1, we tentatively conclude that some effect of limited aspect ratio is responsible for the faster rise rate of $\overline{Z}_p$ and $(\overline{Z_p'^2})^{\frac{1}{2}}$ in case 2. The effect may

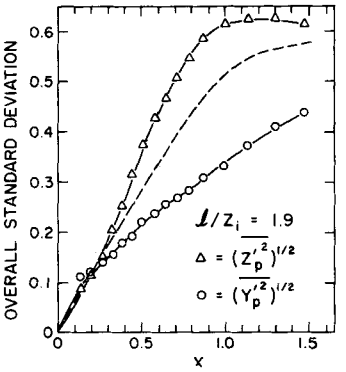

Figure 4. As Fig. 3, but aspect ratio 1·9.

have been associated with the known preference for strong updraughts (rather than downdraughts) to occur along the sidewalls, and to a higher probability for the particle release line (which extended the full length of the chamber) to intercept the sidewall updraught than their compensating downdraughts. Although a factor of about 2 in the turbulence Reynolds number is sacrificed by using case 1 instead of case 2, the effect of a larger aspect ratio is apparently more important in simulating the atmospheric boundary layer. Case 1 also has the additional advantage that the sampling error of a given experiment is only about one-half as large as in case 2.

It is of interest to know how the lateral spread of particles varies in the vertical. In Fig. 5, smoothed values of $(\widetilde{Y_p'^2})^{\frac{1}{2}}$ are plotted versus downstream distance X, where the wavy overbar represents a vertical average over a height interval of $0{\cdot}2z_i$. The $(\widetilde{Y'^2})^{\frac{1}{2}}$ values begin to deviate significantly from each other near $X = 1$ where a relatively large

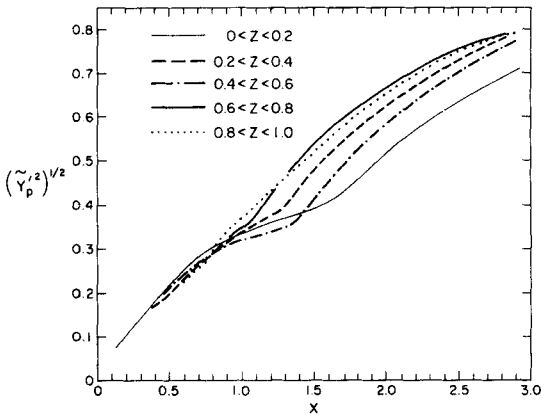

Figure 5. Smoothed dimensionless lateral standard deviations averaged over height interval $0{\cdot}2z_i$ as a function of height and downstream distance for case 1.

number of particles first reach the upper confines of the mixed layer. The lateral spread there increases more rapidly as particles are carried horizontally by the energetic updraught outflows. At larger distances downstream, where the vertical distribution becomes more uniform, the differences between lateral spread at various levels diminishes. The nearly linear section of $(\overline{Y_p'^2})^{\frac{1}{2}}$ which can be noticed in Fig. 3 is more detectable here as a dip in $(\widetilde{Y_p'^2})^{\frac{1}{2}}$ for $z < 0{\cdot}8z_i$ and centred at $X = 1{\cdot}3$.

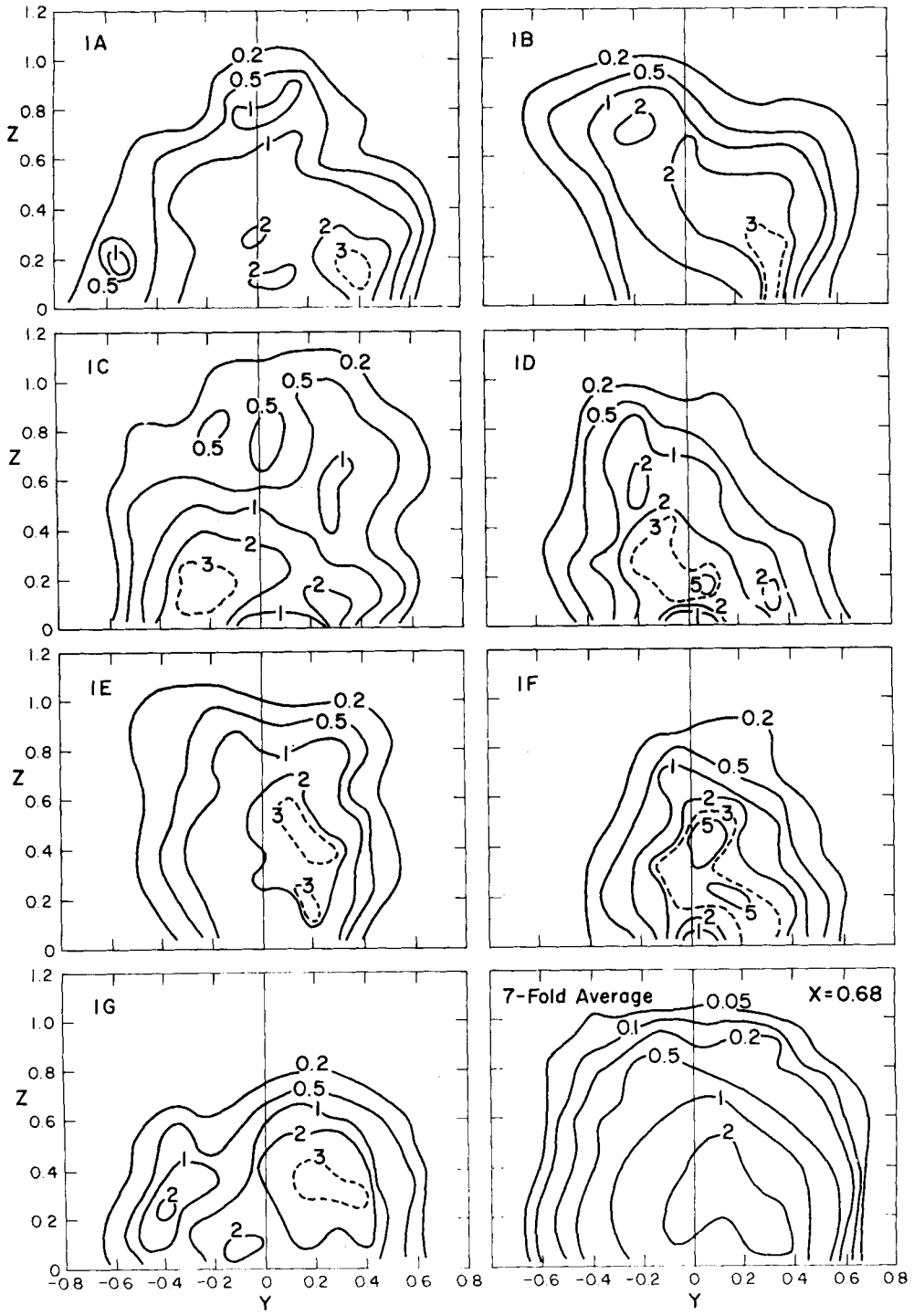

Figure 6. Smoothed contours of dimensionless concentration in the Y–Z plane at $X = 0{\cdot}68$ for the 7 individual experiments A–G of case 1 and the average of A–G.

(*b*) *Representativeness of a single experiment*

It should be noted at this time that results to be presented on concentration distributions will refer only to case 1 with $l/z_i = 4$.

Since the camera viewed the particle release line end-on, a single experiment integrates the effects of turbulent eddies over the length of the release line $4z_i$. This is equivalent to a sampling time $4z_i/U$, which typically has a value of 20–30 min in the atmosphere. Averaging over the 7 laboratory experiments is equivalent in the atmosphere to performing 7 experiments of 20–30 min sampling duration, each having its downwind axis redefined by the 20–30 min mean wind direction and with other scaling parameters determined over the 20–30 min period, before averaging the results together. The main effect of this type of averaging is to decrease further the sampling error by including the influences of a greater range of eddy sizes and locations. These ensemble averaged results will differ distinctly from a single experiment lasting 140–210 min if diurnal/topographical effects with periods significantly longer than $4z_i/U$ are present. To demonstrate differences in concentration that can be expected between individual experiments and the smoothing effect of ensemble averaging over the 7 experiments, smoothed contours of C plotted in the Y–Z plane for an average distance downstream of $X = 0{\cdot}68$ are shown in Fig. 6. The individual experiments are labelled A–G, while the average is labelled '7-fold average'.

Differences in values of C between individual experiments at any location are considerable, indicating the need for a large ensemble of experiments to achieve reliable estimates of concentration. For example, at position $Y = Z = 0{\cdot}4$, values of C vary from 0·4 to 2·2, with the mean being $1{\cdot}13 \pm 0{\cdot}26$. Asymmetries around the release line $Y = 0$ still existing in the 7-fold average are a measure of the remaining sampling error, since in the chamber there should be no preferred horizontal orientation or location of the eddies except close to the sidewalls. (To help ensure such randomness, the convection chamber was designed to have a nearly uniform bottom temperature. Horizontal uniformity of temperature over the entire bottom plate, on both small and large scales, was achieved to within 1·5% of the temperature drop between the surface value and that of the mixed layer.)

(*c*) *Mean concentrations in the X–Z and Y–Z planes*

The dimensionless cross-wind integrated value of C is defined as

$$\bar{C}^Y = \int_{-\infty}^{\infty} C(X, Y, Z)\, dY. \qquad (11)$$

A plot of smoothed values of $\bar{C}^Y$ is presented in Fig. 7. The concentration maximum, occurring initially at release height $z = 0{\cdot}067z_i$, is maintained near that level to a distance downstream of about 0·5. Near $X = 0{\cdot}5$, however, a concentration maximum elevated well above the release height begins to appear. As the particulate plume spreads, the elevated maximum of $\bar{C}^Y$, while decreasing in absolute value, attains a maximum height of about $0{\cdot}8z_i$ near $X = 1{\cdot}5$. Farther downstream the elevated maximum decreases in height and will eventually disappear as the pollutants become well mixed vertically and their concentration approaches the equilibrium value of about 1 (the dimensionless well-mixed value would be exactly 1 if no particles appeared at heights $z > z_i$).

Smoothed contours of the centreline concentration $C(X, 0, Z)$ are presented in Fig. 8. The elevated concentration maximum also appears for these centreline concentrations, with the general features of the contour shapes being similar to those for $\bar{C}^Y$. However, it is interesting to note that the height of the maximum concentration here does not exceed $z = 0{\cdot}65z_i$, compared with $z \simeq 0{\cdot}8z_i$ for $\bar{C}^Y$. This probably indicates that the particles

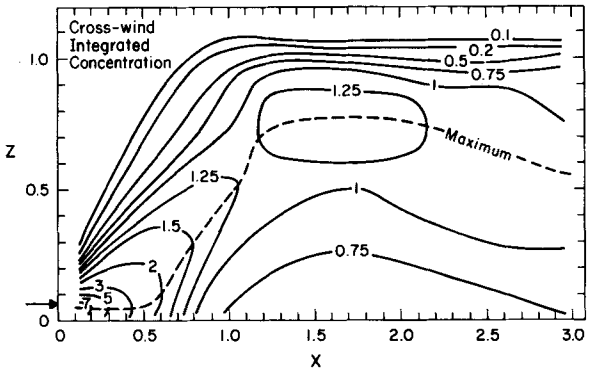

Figure 7. Smoothed values of dimensionless cross-wind integrated concentration as a function of height and downstream distance. Arrow denotes source location.

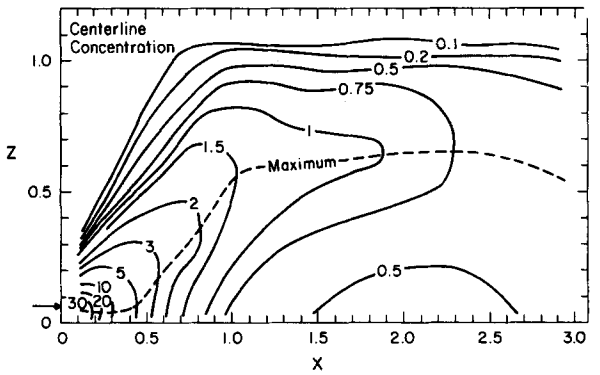

Figure 8. Smoothed values of dimensionless centreline concentration as a function of height and downstream distance. Arrow denotes source location.

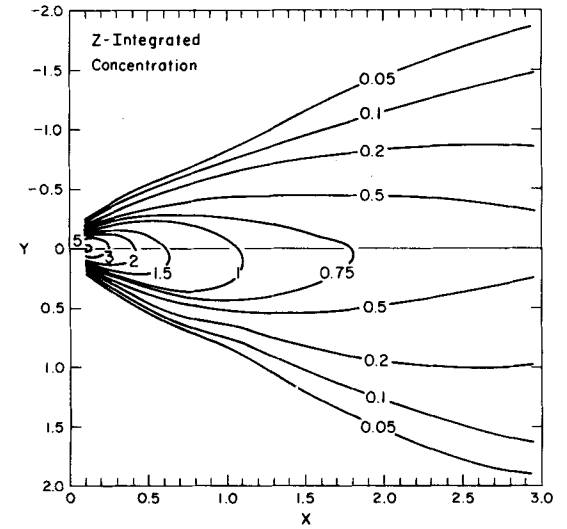

Figure 9. Smoothed values of dimensionless Z-integrated concentration as a function of lateral distance and downstream distance.

carried rapidly upwards for $X < 1$ are soon dispersed outwards in $\pm y$, where they contribute more heavily to $\bar{C}^Y(X,Z)$ than to $C(X,0,Z)$ at large Z.

Smoothed values of the Z-integrated concentrations are shown in the X–Y plane in Fig. 9. Asymmetries in concentration about the release line $Y = 0$ develop as the ensemble-averaged plume spreads. Farther downstream, where the particles have had greater opportunity to become incorporated into adjacent eddies, the distribution in Y becomes more symmetrical. Therefore we believe that the asymmetry at intermediate distances is a reflection of sampling error.

(*d*) *Best-fit Gaussian distributions to the concentration data*

The Gaussian distribution function has long provided a mathematical model for diffusion from a CPS in the atmosphere (e.g. Sutton 1932), and many experiments in the atmospheric surface layer have indicated that the Gaussian plume formula has a wide range of practical applicability (Pasquill 1962). The attractiveness of this approach to diffusion problems is due, of course, to its simplicity in that when the diffusion parameters σ_y and σ_z are known or can be estimated, then with use of measurements of source strength or the ground-level centreline concentration, the complete concentration field becomes specified. It is therefore of great interest to determine how closely the laboratory model supports the Gaussian assumption.

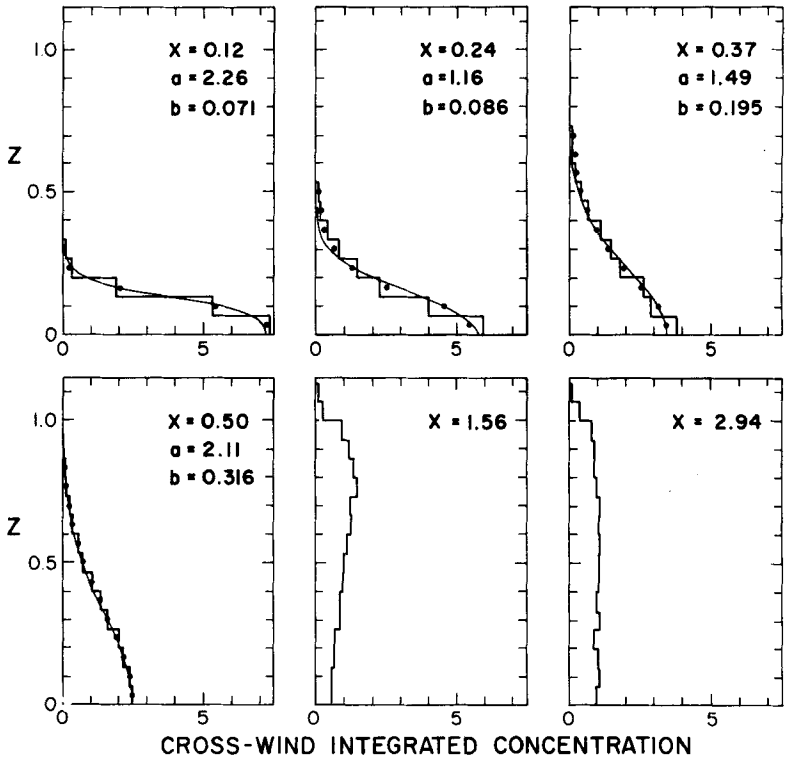

Figure 10. Observed vertical distribution of dimensionless cross-wind integrated concentration – histogram; best-fit Gaussian distribution – solid curve; best-fit distribution from equation (12) with values of exponent a and adjustable parameter b as labelled – closed circles. All shown for various values of X.

Comparisons have been made between the concentration probability distributions of the model and Gaussian distributions. In Fig. 10 the vertical distributions of $\bar{C}^Y$ are plotted

as histograms for various values of X. The smooth curves are the best-fit Gaussian profiles with perfect reflection at the lower boundary, calculated by use of

$$\bar{C}^Y = C_0\left[\exp -\left(\frac{Z+Z_r}{\sqrt{2}.b}\right)^a + \exp -\left|\frac{Z-Z_r}{\sqrt{2}.b}\right|^a\right] \quad . \quad . \quad (12)$$

with $a = 2$, in which case b becomes the Gaussian vertical standard deviation σ_Z. In (12), C_0 is proportional to the vertically summed concentration. The closed circles are points from the solution of (12) where a and b were determined by minimizing the r.m.s. deviations from the observed concentrations. For the atmospheric surface layer under unstable conditions Elliott (1961) has analysed data from a near ground-level release, and using a form of (12) found a to be slightly less than 1·5. The values of best fit as from this study fall in the range 1·1–2·3 for $X < 0{\cdot}5$ with no simple systematic variation with X. Inspection of Fig. 10 does indicate though that there is very little practical difference in predicted concentrations whether $a = 1{\cdot}2$ or 2, with b free to be adjusted. Thus the Gaussian formulation adequately represents our observed laboratory vertical distributions of $\bar{C}^Y$ out to $X = 0{\cdot}5$. For values of $X > 0{\cdot}5$ the elevated maximum becomes apparent, and no Gaussian formulation with a near-surface release can properly predict this feature. The elevated concentration maximum achieves the greatest prominence near $X = 1{\cdot}56$, where it is about 2·5 times larger than the surface value at that X. The final plot in Fig. 10 indicates that the concentration distribution is essentially well mixed vertically by $X = 2{\cdot}94$.

Use of the Gaussian formulation for vertical concentration distributions requires knowledge about σ_Z. From our measurements, $(\overline{Z_p'^2})^{\frac{1}{2}}$ is known, but is strictly equal to σ_Z only for a Gaussian distribution and for a ground release. For an elevated source $(\overline{Z_p'^2})^{\frac{1}{2}}$ and σ_Z are not identical, but can be related through a formula depending on Z given by

$$\overline{Z_p'^2} = \sigma_Z^2 - 4Z_r\sigma_Z\eta + 2Z_r^2(1-2A) \quad . \quad . \quad (13)$$

where η is the ordinate of the dimensionless normal curve at Z_r/σ_Z, and A is the area under the normal curve out to Z_r/σ_Z. The relationship described by (13) is shown in a universal-type plot in Fig. 11 (the same equation can be used in dimensional form in which case knowledge of z_i is not required). When Z_r and $(\overline{Z_p'^2})^{\frac{1}{2}}$ are known and the Gaussian assumption for the vertical concentration distribution can be made, then σ_Z can be determined by use of the curve in Fig. 11. Eq. (13) incorporates the assumption of perfect reflection at the lower boundary but does not include reflection at z_i. Thus use of (13) or the curve of Fig. 11 should be limited to downstream distances for which z_i has not yet become important.

The best-fit Gaussian distributions in Y are compared to the folded histogram data in Fig. 12 for two values of X and for height intervals of $0{\cdot}2\,z_i$. For small values of X, where particles have not spread much, the Gaussian formulation appears adequate. At $X = 0{\cdot}56$, however, an excess of particles compared with the best Gaussian fit, exists for

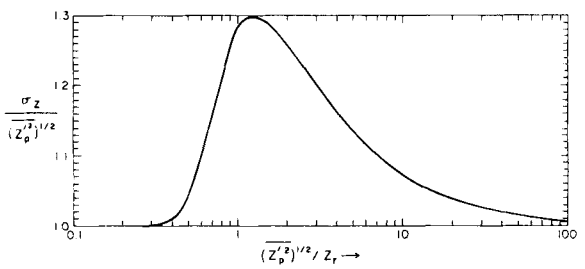

Figure 11. Dependence on release height of predicted Gaussian vertical standard deviation and observed particle vertical standard deviation.

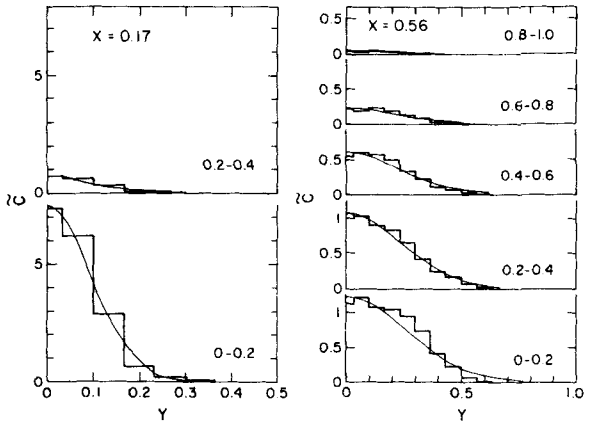

Figure 12. Lateral distribution of dimensionless Z-integrated concentration over height interval $0{\cdot}2z_i$ and folded around $Y = 0$ – histogram; best-fit Gaussian distribution – solid curve. Both shown for two values of X.

$0{\cdot}1 \leqslant Y \leqslant 0{\cdot}3$. This particle excess is associated with the concentration maximum being displaced slightly to one side of the instantaneous release line, as in Fig. 9. This same feature is also readily apparent somewhat farther downstream as evidenced by Fig. 13 where the common Gaussian-type plot is used for the unfolded data. At $X = 2{\cdot}63$, however, the particles are seen to be more symmetrically distributed. Since the asymmetry in the Y-distribution has been ascribed to sampling error, the Gaussian formulation appears to be an adequate estimator of the lateral distribution for all $X < 3$. A parameterization by Deardorff and Willis (1975) of these laboratory model concentration distributions therefore incorporates the Gaussian formulation for the lateral spread.

(e) *Comparison with atmospheric diffusion parameters*

Since the term w_*/U serves as the stability parameter in this study it is of interest to relate it to a more commonly measured parameter, such as the r.m.s. vertical wind angle

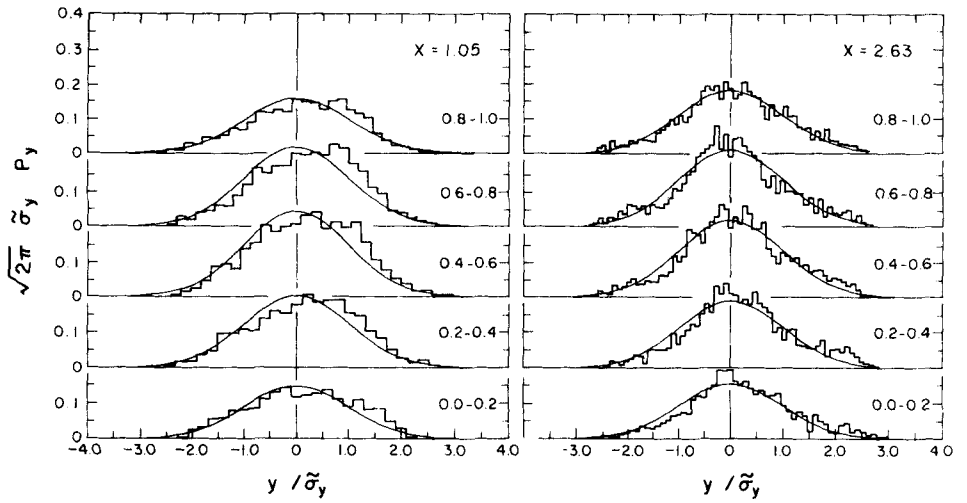

Figure 13. Particle lateral displacement probability distribution for height intervals $0{\cdot}2z_i$ as a function of lateral distance from release line $Y = 0$ – histogram; best-fit Gaussian distribution – solid curve. Both shown for two values of X.

σ_ϕ. If the r.m.s. vertical velocity fluctuation, σ_w, is measured in the convective surface layer at a height greater than about $-0{\cdot}5L$ where L is the Monin–Obukhov length, it will be found to be given by (Wyngaard *et al.* 1971)

$$\sigma_w = 1{\cdot}34(z/z_i)^{\frac{1}{3}}w_* \quad . \quad . \quad . \quad (14)$$

where z is the height of measurement. Upon approximating σ_ϕ by

$$\sigma_\phi \simeq \sigma_w/U \quad . \quad . \quad . \quad . \quad (15)$$

and substituting (15) into (14), we find

$$w_*/U = 0{\cdot}75(z/z_i)^{-\frac{1}{3}}\sigma_\phi. \quad . \quad . \quad . \quad (16)$$

Since w_*/U is not a function of height, (16) reminds us that σ_ϕ increases as $z^{\frac{1}{3}}$ in the convective surface layer. Therefore, in use of (16), the height at which σ_ϕ is measured, relative to z_i, should be taken into consideration even though the factor $(z/z_i)^{-\frac{1}{3}}$ is usually confined between the limits of 2 and 10.

The elevated-source short-range diffusion measurements of Islitzer (1961) for unstable atmospheric conditions provide sufficient information to make a comparison with the model results. Islitzer related wind fluctuation data to measurements of the diffusion parameters and expressed the lateral diffusion by

$$\sigma_y = (\sigma_\theta/1{\cdot}23)x, \quad . \quad . \quad . \quad (17)$$

where σ_θ is the r.m.s. azimuthal wind angle. He reported values of both σ_θ and σ_ϕ; the diffusion measurements extended over the downstream range 150–1800 m.

By inspection of the vertical velocity spectra of Kaimal *et al.* (1972) we estimate that Islitzer, who used a 5-second averaging period, underestimated the true σ_ϕ by about 8%. With the aid of the corrected measurements of σ_ϕ and direct estimates of $z_i \simeq 2{\cdot}2$ km at the same site by Angell (1972), we find from application of (16) that $w_*/U \simeq 0{\cdot}31$ for Islitzer's average atmospheric conditions. This result, which permits (17) to be expressed in terms of our X upon use of Islitzer's measurements of σ_ϕ, provides a basis for direct comparison with our model data. In a similar manner we can also compare the laboratory data with the ground-source lateral diffusion measurements of Islitzer and Dumbauld (1963), where their observations extended from $x = 100$ to 3200 m. In this case the correction to σ_ϕ was 18%, and w_*/U again turned out to be 0·31. However, an additional uncertainty exists for this comparison since their σ_θ measurements were made at a small value of $-z/L$ that we estimate to be about 0·2. Their best-fit power law can be expressed in terms of the parameters used in this study as

$$\sigma_Y = 0{\cdot}37X^{0{\cdot}86}. \quad . \quad . \quad . \quad (18)$$

The comparisons are shown in Fig. 14 between the atmospheric observations of ground-arc lateral spread and our laboratory near-surface values of $(\widetilde{Y_p'^2})^{\frac{1}{2}}$ for which $0 < Z < 0{\cdot}2$. The dotted line is from the short-term relationship

$$(\widetilde{Y_p'^2})^{\frac{1}{2}} = (\sigma_v/w_*)_r X, \quad . \quad . \quad . \quad (19)$$

where the value of the dimensionless r.m.s. lateral velocity fluctuation at release height, $(\sigma_v/w_*)_r$, was determined from Willis and Deardorff (1974, Fig. 6). There is good overall agreement between the atmospheric and model data, with the power-law expression of Islitzer and Dumbauld providing the closer approximation. The region for which the comparison is closest appears limited to $0{\cdot}2 < X < 0{\cdot}4$. The lack of such agreement for distances outside of this range can be attributed, at least in part, to the requirement placed

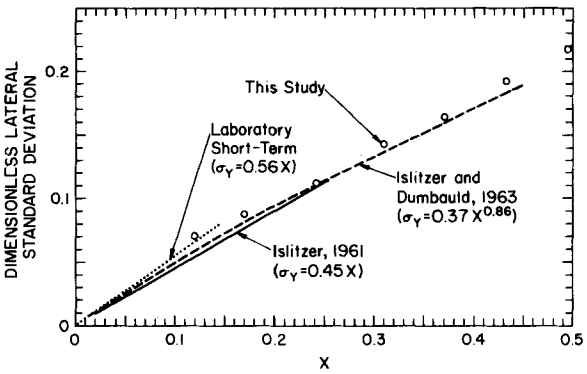

Figure 14. Dimensionless low-level lateral standard deviations. Solid line – atmospheric observations of Islitzer (1961); dashed line – atmospheric observations of Islitzer and Dumbauld (1963); dotted line – laboratory short-term diffusion formulation as expressed by Eq. (18); open circles – our laboratory data

on the atmospheric data that a single functional form describe the lateral spread from near the release point to a downstream distance of $X \simeq 0{\cdot}5$. In contrast, the laboratory data suggest that the short-range lateral spread can be closely represented by an initial linear segment in the region $0 < X < \sim 0{\cdot}15$ and then, as noted previously, by $(\widetilde{Y_p'^2})^{\frac{1}{2}} = 0{\cdot}38X^{0{\cdot}83}$ in the range $0{\cdot}2 < X < 0{\cdot}8$. A comparison between σ_Zs is not made here since the release heights used for the atmospheric observations are considerably less than the model value of $0{\cdot}067z_i$ (Islitzer 1961: $z_r \simeq 0{\cdot}02z_i$; Islitzer and Dumbauld 1963: ground release), and the effects of release height on the short-range vertical spread are much more significant than upon the lateral spread.

It is also of interest to compare w_*/U values with the frequently used stability categories of the Brookhaven Laboratories (Singer and Smith 1966) and of Pasquill-Gifford (Pasquill 1961; Gifford 1961). If atmospheric data are not available to compute directly w_*/U values or to estimate them as outlined by Eqs. (14)–(16), then use of a more tenuous approach in

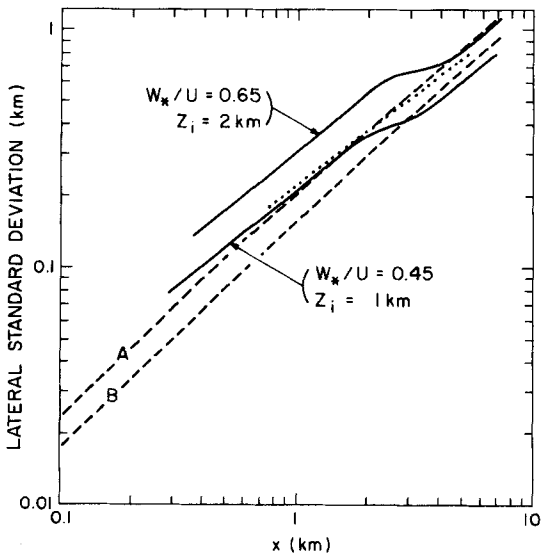

Figure 15. Dimensional low-level lateral standard deviations as derived from laboratory data for $w_*/U =$ 0·65 and 0·45. Values from Pasquill–Gifford stability classes A and B – dashed lines. Values from class B′ of McElroy (1969) – dotted curve.

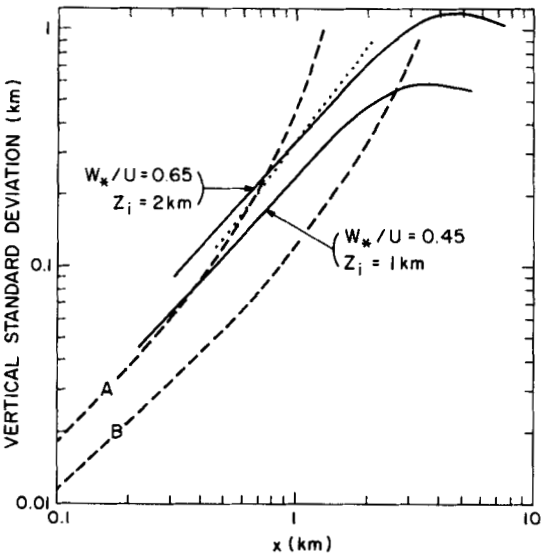

Figure 16. Dimensionless vertical standard deviations as derived from laboratory data for $w_*/U = 0{\cdot}65$ and 0·45. Values from Pasquill–Gifford stability classes A and B – dashed lines. Values from B′ of McElroy (1969) – dotted curve.

estimating them becomes necessary. In relating w_*/U values to the Pasquill–Gifford classes A and B, one such approach is: 1) to take typical values of $-L$, as estimated by Pasquill and Smith (1972) to be 2–3 m for class A and 4–5 m for class B; 2) to assume a reasonable mixed-layer depth, for example, 2 km for class A and 1 km for class B; and 3) to assume a typical value for the resistance coefficient, $u_*/U = 0{\cdot}05$, for both classes A and B. With use of these values one arrives at the rounded-off values of $w_*/U = 0{\cdot}65$ for class A and 0·45 for class B. Somewhat different value for w_*/U would be obtained if instead one begins with the relationship

$$\sigma_\theta = (\sigma_v/w_*)(w_*/U) \quad . \quad . \quad . \quad (20)$$

and uses values of the r.m.s. lateral velocity fluctuation from Willis and Deardorff (1974, Fig. 6), and the stability class-σ_θ association of Slade (1966).

Near-ground-level values of $(\widehat{Y_p'^2})^{\frac{1}{2}}$ taken from Fig. 5 are plotted in comparison with the Pasquill–Gifford curves of classes A and B in Fig. 15, and $(\overline{Z_p'^2})^{\frac{1}{2}}$ values taken from Fig. 3 are plotted in Fig. 16 (for comparison with atmospheric values the latter, if desired, can be converted to reflected-image σ_Z values through use of Fig. 11). It is seen that only fair agreement exists between the model values and the original stability-class curves. Results from urban area diffusion measurements as presented by McElroy (1969) are also plotted in the figures as the dotted curves for his most unstable case B′. The latter curves are in better agreement with the model values, lying mostly between the laboratory estimates for classes A and B, and having a similar slope.

Estimates of appropriate values of w_*/U for the Brookhaven gustiness classes B_2 and B_1 have been made through use of (20) and the σ_θ measurements of Singer and Smith (1966). Rounded-off values arrived at through this approach are $w_*/U = 0{\cdot}55$ for B_2 and 0·25 for B_1.

Values of the lowest-level $(\widehat{Y_p'^2})^{\frac{1}{2}}$ and of $(\overline{Z_p'^2})^{\frac{1}{2}}$ from the model are plotted in Figs. 17 and 18, respectively, as solid lines in comparison with the values of Brookhaven gustiness classes B_2 and B_1 (dashed lines). Considering the uncertainties involved in our estimates

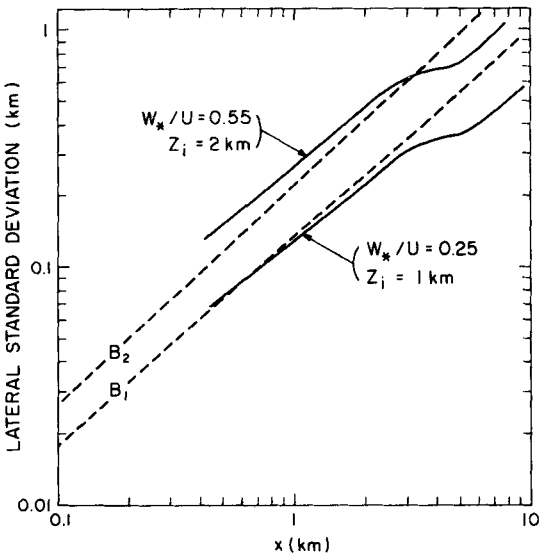

Figure 17. Dimensionless low-level lateral standard deviations as derived from the laboratory data for $w_*/U = 0{\cdot}55$ and $0{\cdot}25$. Values for Brookhaven gustiness classes B_2 and B_1 – dashed lines.

of proper values of w_*/U for classes B_2 and B_1, reasonable agreement exists between the model and the Brookhaven results. Although slopes of the Brookhaven values are somewhat different than those from the model, the overall agreement appears better than for the Pasquill–Gifford classes A and B. However, close agreement with past class A–B data may be fortuitous, since diffusion data which were lumped together within any particular stability class encompass a miscellany of unknown w_*/U values and unknown z_i values. In the future it is to be hoped that high quality diffusion data will be accompanied by representative measurements of the surface heat flux, z_i, and U, or alternatively of z_i and σ_ϕ at a known height in the surface layer.

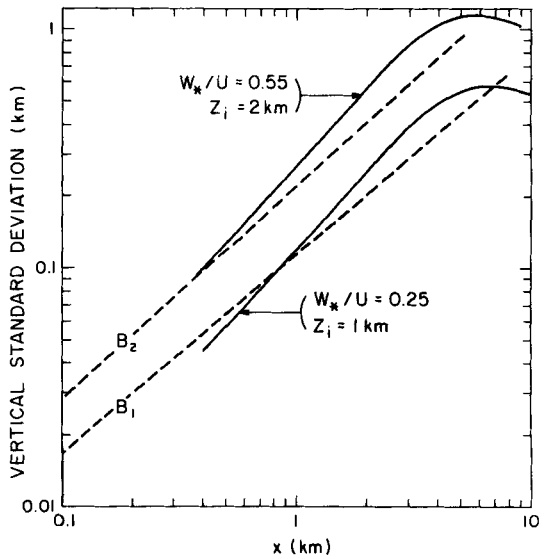

Figure 18. Dimensionless vertical standard deviations as derived from the laboratory data for $w_*/U = 0{\cdot}55$ and $0{\cdot}25$. Values for Brookhaven gustiness classes B_2 and B_1 – dashed lines.

(*f*) *Applications and limitations of the model results*

The present laboratory results are most applicable for either an instantaneous-line source or continuous-point-source release at a height $z = 0{\cdot}067 z_i$. For release heights approaching ground level we estimate that the present results apply approximately for $X > 0{\cdot}5$. Their use is most appropriate for a release of neutrally buoyant, inert pollutants over flat terrain into a clear-air convective planetary boundary layer when the mean wind is in the range of 3–12 m s^{-1}. The upper limit of U here, or more properly in (3), corresponds to the requirement $-L < 0{\cdot}1 z_i$.

The Gaussian distribution functions provide a reasonably good practical approximation to the observed concentration distributions in Y, at least for $0{\cdot}15 \leqslant X \leqslant 3$, and in Z for $0{\cdot}15 \leqslant X \leqslant 0{\cdot}5$. At a value of X exceeding about 0·5, the elevated concentration maximum precludes further use of the Gaussian plume model to describe the Z-distribution. The limiting effect of the capping inversion upon the vertical diffusion becomes apparent by $X \simeq 0{\cdot}8$. The concentration distribution is essentially uniform within the mixed layer for dimensionless downstream distances exceeding $X \simeq 2{\cdot}5$.

The use of w_*/U as a stability parameter for the more unstable conditions, rather than stability or gustiness classes, is recommended if the surface heat flux, mixed-layer depth, and representative mean wind are known. A valid simpler approach, Eq. (16), for estimating w_*/U values during diffusion measurements require observations only of the mixed-layer depth and the r.m.s. vertical wind angle at a known height.

Limitations imposed by inequalities (3) and (7) together give $0{\cdot}2 < x/z_i < 18$ for the maximum downstream range over which the model results apply.

References

Angell, J. K.	1972	A comparison of circulations in transverse and longitudinal planes in an unstable planetary boundary layer, *J. Atmos. Sci.*, **29**, pp. 1252–1261.
Arya, S. P. S. and Wyngaard, J. C.	1975	Effect of baroclinicity on wind profiles and the geostrophic drag law for the convective planetary boundary layer, *Ibid.*, **32**, pp. 767–778.
Deardorff, J. W.	1970	Convective velocity and temperature scales for the unstable planetary boundary layer and for Rayleigh convection, *Ibid.*, **27**, pp. 1211–1213.
	1972	Numerical investigation of neutral and unstable planetary boundary layers, *Ibid.*, **29**, pp. 91–115.
Deardorff, J. W. and Willis, G. E.	1974a	Computer and laboratory modelling of the vertical diffusion of nonbuoyant particles in the mixed layer, *Adv. in Geophys.*, 18B, Academic Press, pp. 187–200.
	1974b	Physical modelling of diffusion in the mixed layer, *Symp. on Atmos. Diff. and Air Poll.*, Santa Barbara, Calif., published by Amer. Met. So., Boston, Mass., pp. 387–391.
	1975	A parameterization of diffusion into the mixed layer, To appear in *J. Appl. Met.*
Elliott, W. P.	1961	The vertical diffusion of gas from a continuous source, *Int. J. Air and Water Poll.*, **4**, pp. 33–46.
Gifford, F. A.	1961	Use of routine meteorological observations for estimating atmospheric dispersion, *Nuclear Safety*, **2** (4), pp. 47–51.
Islitzer, N. F.	1961	Short-range atmospheric dispersion measurements from an elevated source, *J. Met.*, **18**, pp. 443–450.
Islitzer, N. F. and Dumbauld, R. K.	1963	Atmospheric diffusion-deposition studies over flat terrain; *Int. J. Air and Water Poll.*, **7**, pp. 999–1022.
Kaimal, J. C., Wyngaard, J. C., Izumi, Y. and Coté, O. R.	1972	Spectral characteristics of surface-layer turbulence, *Quart. J. R. Met. Soc.*, **98**, pp. 563–589.
Lamb, R. G., Chen, W. H. and Seinfeld, J. H.	1974	Numerico-empirical analyses of atmospheric diffusion theories, *J. Atmos. Sci.*, **32**, pp. 1794–1807.

McElroy, J. L. 1969 A comparative study of urban and rural dispersion. *J. Appl. Met.*, **8**, pp. 19–31.

Pasquill, F. 1961 The estimation of the dispersion of windborne material, *Met. Mag.*, **90** (1063), pp. 33–49.

1962 *Atmospheric diffusion*, D. van Nostrand, London.

Pasquill, F. and Smith, F. B. 1970 The physical and meteorological basis for the estimation of the dispersion of windborne material, *Proc. Second Intern. Air Poll. Conf.*, New York, Academic Press.

Singer, I. A. and Smith, M. E. 1966 Atmospheric dispersion at Brookhaven National Laboratory, *Int. J. Air and Water Poll.*, **10**, pp. 125–135.

Slade, D. H. 1966 Estimates of dispersion from pollutant releases of a few seconds to 8 hours in duration, *ESSA-TN-39-ARL-3*, April.

Sutton, O. G. 1932 A theory of eddy diffusion in the atmosphere, *Proc. Soc. London*, A., **135**, pp. 143–165.

Willis, G. E. and Deardorff, J. W. 1974 A laboratory model of the unstable planetary boundary layer, *J. Atmos. Sci.*, **31**, pp. 1297–1307.

Wyngaard, J. C., Coté, O.R. and Izumi, Y. 1971 Local free convection, similarity, and the budgets of shear stress and heat flux, *Ibid.*, **28**, pp. 1171–1182.

Yaglom, A. M. 1971 Turbulent diffusion in the surface layer of the atmosphere, *Izv. Acad. Sci., USSR, Atmos. Oceanic Phys.*, **8**, pp. 333–340.